Desalination 249 (2009) 416–422

Contents lists available at ScienceDirect

Desalination

journal homepage: www.elsevier.com/locate/desal

3-D Monte Carlo simulation of particle deposition on a permeable surface

Yanling Li, Nam Vu, Albert S. Kim *

Civil and Environmental Engineering, University of Hawaii at Manoa, 2540 Dole Street, Honolulu, HI 96822, USA

ARTICLE INFO

Article history:
Accepted 28 May 2009
Available online 2 October 2009

Keywords:
Particle trajectory and deposition
Fractal dimension
Permeable surface and membrane
Monte Carlo simulation
Penetration depth

ABSTRACT

Monte Carlo simulations are performed to investigate deposition phenomena of sticky particles that undergo diffusive, convective, and gravitational influences on a highly permeable surface. Deposited structures are studied in 3-D space using a Pelcet number as the key parameter. Fractal dimensions of the particle trajectory and deposit structure indicate that a transition from diffusion-limited to convection (and gravitation)-limited transport occurs at the Peclet number of $Pe = 10^{-0.84} = 0.146$. Analysis of the lateral density shows three distinct regions of deposit structures (defined in this study): founding, grown, and progressing regions. A penetration depth is defined to explain the relationship between particle transport and the evolution of deposit structures.

1. Introduction

The deposition of particles (including biocolloids) on permeable surfaces plays an important role in natural and engineered processes influenced by a variety of physical, chemical and biological conditions. When rigid particles are filtered using membranes, permeate flow drags particles down toward the membrane surface, and particle transport is primarily affected by Brownian diffusion, fluid flow, gravitational force, and interparticle interactions [1,2]. When the suspension has a low concentration of strongly attractive (sticky) particles, deposit layers are formed through sequential capturing of drifting particles by pre-deposited particles. Particle deposition and aggregation effectively control the performance of membrane filtration [3–7] and significantly affect the growth and morphology of deposit structures. The geometrical complexity of the structures is described by non-integer fractal dimensions [8–11]. This characteristic fractal nature in particle deposition was successfully modeled and explained by Barabsi and Stanley [12].

Several researchers performed computer simulations to study the deposition behavior of mono- and poly-dispersed particles and characterized the deposit morphology using the fractal dimension concept [13–15]. Veerapaneni and Wiesner [13] used a biased Monte Carlo simulation to study particle deposition in two dimensional space under random Brownian motion as well as convective and gravitational influences. Due to the geometrical constraint of their simulations performed in 2-D Euclidian dimensions, Veerapaneni and Wiesner's results primarily provide qualitative insights into the real observation of particle transport and deposit morphology physically occurring in 3-D space. Although some studies engaged 3-D modeling [16–19], they included only the diffusion-limited transport in various circumstances in the absence of a unidirectional bias such as convection and/or gravitation. Therefore, we extended Veerapaneni and Wiesner's model to a 3-D simulation, incorporating the Peclet number, defined as the ratio of downward convective and gravitational flux to the upward diffusive flux, and investigated particle transport phenomena under multiple influences including diffusion.

The morphology of cake structure varies with the potential energy, shape, size and rigidity of colloidal particles. During filtration processes, colloidal particles may undergo adsorption of organic matter on their surfaces, which alters the interparticle interactions. Furthermore, deformability and eccentricity of the organic matter influences cake compressibility, permeability, and morphology. In this case, effects of organic matter in the feed solution on cake formation and membrane fouling can be studied by employing phenomenological potential functions between two colloids, as is also possible for soft particles. Nevertheless, particle transport influenced by strong attractive interparticle interactions and external (e.g., hydrodynamic and gravitational) forces should exist amidst the diffusion-limited and convection/gravitation-limited transport regimes. Therefore, this study focuses on advances in 3-D simulation of rigid particle deposition followed by structural evolution without restructuring during dead-end filtration, where the membrane is portrayed as a highly permeable substrate [13]. The present model covers pure diffusion-limited (entropic) to convection-limited (ballistic) transport, which are ideally characterized as zero and infinite Peclet numbers, respectively. The model is capable of achieving a consistent and integrated view of deposition phenomena of rigid, sticky particles in 3-D space and investigating the filtration behavior under a wide range of operating conditions. Moreover, a novel characteristic parameter, denoted here as penetration depth, is introduced to clarify

* Corresponding author. Tel.: +1 808 956 3718; fax: +1 808 956 5014.
E-mail addresses: yanlingl@hawaii.edu (Y. Li), namvu@hawaii.edu (N. Vu), AlbertSK@hawaii.edu (A.S. Kim).
URL: http://pam.eng.hawaii.edu (A.S. Kim).

0011-9164/$ – see front matter © 2009 Elsevier B.V. All rights reserved.
doi:10.1016/j.desal.2009.05.018

how the top-surface of the deposit structure evolves under a certain transport regime.

2. Monte Carlo simulations

2.1. Simulation method

Following Meakin's work on a lattice-based model [8,17,20], we performed Monte Carlo simulations of particle deposition on a highly permeable surface in a normal flow field. The rectangular simulation box has dimensions of $L\times W\times H$, where L (=300) and W (=300) are the length and width of the permeable square substrate, and H (=800) is the box height. The distance unit between the two nearest grid points in each coordinate is the particle diameter, d_p. A simulation starts with releasing the first particle at 150 grid points above the bottom of the simulation box and traces the trajectory until it reaches the substrate surface. When pre-deposited particles are present, a new particle is released 150 grid points above the top-most particle (i.e., highest z-coordinate). The released particle can move in one of six directions (i.e., $\pm x$, $\pm y$, and $\pm z$) at each step movement. The probability for the particle to move in the $-z$ direction is biased due to the downward fluid flow and gravitational force toward the permeable substrate. The probabilities in the other five directions (i.e., $\pm x$, $\pm y$, and $+z$) are evenly distributed [13]:

$$P_i = \frac{1+\mathrm{Pe}}{6+\mathrm{Pe}} \quad \text{for} \quad i=-z \tag{1a}$$

$$P_i = \frac{1}{6+\mathrm{Pe}} \quad \text{for} \quad i=\pm x,\pm y,+z \tag{1b}$$

where Pe is the Peclet number, and P_i is the probability that a particle moves in the i-direction. The Peclet number is defined as

$$\mathrm{Pe} = \frac{V_c+V_g}{V_d} \tag{2}$$

with

$$V_d = \frac{k_B T}{3\pi d_p^2 \mu} \tag{3}$$

$$V_g = \frac{d_p^2 g(\rho_p-\rho_f)}{18\mu} \tag{4}$$

where V_c, V_d, and V_g are velocities representing convective, diffusive, and gravitational transports, respectively; g is the gravitational acceleration; ρ_p and ρ_f are mass densities of particle and fluid, respectively; μ is the pure fluid viscosity; k_B is the Boltzmann constant; and T is the absolute temperature. Directions of V_c and V_g are downward, and that of V_d is upward. If the diffusion is negligible due to a fast flow and/or significant gravitational effects (based on density and size differences between particles), then the Peclet number diverges to infinity, giving the probability of

$$P_i \cong \begin{cases} 1 & i=-z \\ 0 & \text{otherwise} \end{cases}. \tag{5}$$

Thus, the transport is convection/gravitation-limited and the trajectory of particles, once released, is similar to rain drops falling to the ground in the normal direction (i.e., ballistic movement). If the particle size is small enough, then Pe is close to zero, providing a uniform probability distribution in each of the six directions:

$$P_i \approx \frac{1}{6} \quad \text{for} \quad i=\pm x,\pm y,\pm z. \tag{6}$$

In this case, until the particle deposits on the substrate or onto one of the pre-deposited particles, the transport of the drifting particle is diffusion-limited and almost identical to a random walk movement in 3-D space.

2.2. Speedup algorithm

The core computational task of this Monte Carlo simulation is to verify whether the drifting particle is in contact with the substrate surface and/or any of the pre-deposited particles. This procedure requires calculation, at each simulation step, of all the pair distances between the drifting particle and deposited particles, as well as finding the minimum distance to the drifting particle. The distance from the substrate to the center of the drifting particle is equal to the z-coordinate of the particle. The number of deposited particles linearly increases as the simulation continues, as does the number of the pairs. In a later stage of the simulation, calculations of all of pair distances required impractical CPU time, especially under diffusion-limited transport. To reduce the heavy computational tasks, a cutoff algorithm was developed to speed up the simulations according to the following.

When a drifting particle is initially released at $\vec{r}_{ini} = (i_{ini}, j_{ini}, k_{ini})$, the location of a pre-deposited particle that has the shortest distance to the released particle, $\vec{r}_p = (i_p, j_p, k_p)$, provides

$$\vec{r}_{ini}-\vec{r}_p = \sqrt{(i_{ini}-i_p)^2+(j_{ini}-j_p)^2+(k_{ini}-k_p)^2} \tag{7}$$

denoted as the cutoff distance. Here, it is worth noting that the drifting particle should move at least

$$N_{free} = |i_{ini}-i_p| + |j_{ini}-j_p| + |k_{ini}-k_p| - 1$$

times to be at a distance from the released point equivalent to the cutoff distance or to have contact with the deposited particle located at $\vec{r}_p$. Note that diagonal movements are not allowed in this simulation. During these N_{free} times of movement, the drifting particle will never have any collision opportunities with any of the deposited particles on the membrane surface but only performs the biased random walk in 3-D space, which is governed by the probability of Eqs. (1a) and (1b). This indicates that the calculation of pair distances from the drifting particle to all pre-deposited particles is unnecessary within the N_{free} steps. After N_{free} times of free drifting, $\vec{r}_p$ is updated with the location of a new particle, which gives a new cutoff distance to the drifting particle that just finished N_{free} movements.

Using this cutoff algorithm, we obtained a significant increase in speed in the 3-D deposition simulations: on average, each simulation took two or three weeks for the top-most particle to reach the ceiling of the simulation box (i.e., $H=800$). Without utilizing the cutoff distances, 3-D simulations with a reasonable number of particles is a formidable task. Simulations with low Peclet numbers took longer than those of high Peclet numbers because the diffusion-limited mechanism allowed more random-walk-like movements of the particles, and therefore drifting particles stayed longer in the bulk phase before deposition. A series of simulations were conducted using a Beowulf PC cluster (Dell Inc.) consisting of 16 nodes, each having two 2.3 GHz Xeon processors and 2 GB of random access memory. Flexible and efficient memory handling for the increasing number of deposited particles was possible using the dynamic memory allocation (DMA) features of FORTRAN 90 [21]. A queuing system, Load Sharing Facilities (LSF) (Platform Computing Inc.), was used to run and manage the large-scale simulation tasks in a stable and optimized manner.

2.3. Conditions

The following conditions were used to perform the MC simulations to generate fractal deposit structures for given Peclet numbers.

2.3.1. Perfect sink

Pre-deposited particles and substrate surfaces commonly play the role of a perfect sink to drifting particles, whose movements are governed by the directional probability defined in Eq. (1). Once a drifting particle arrives at and sticks to the substrate surface or any of the pre-deposited particles, its detachment and re-suspension to the bulk phase are prohibited. Then, the number of deposited particles increases by one (i.e., $N_p \rightarrow N_p + 1$), and a new particle is released 150 grid points above the top-most particle of the updated deposit structure that includes the just-deposited particle. This perfect sink is analogous to the case where the sticking probability is one. Effects of the sticking probability (i.e., collision efficiency) on deposit morphology can be found elsewhere [8,22,23].

2.3.2. Lateral boundary

The periodic boundary condition [20,22] is used on the four wall sides of the simulation box: if a particle exits at $x = \pm L/2$ (or $y = \pm L/2$), it reenters at $x = \mp L/2$ (or $y = \mp L/2$). This boundary condition is to mimic global homogeneity and translational invariance of the deposit structure in the lateral plane. Veerapaneni and Wiesner [13] used the reflecting boundary condition by which, if a particle escapes from a simulation wall, it bounces back into the simulation grid near the reflecting wall. For a wide enough substrate, the periodic and reflecting boundary conditions would not provide a significant difference in deposit structures. However, the periodic boundary condition implies infinite homogeneity and translational invariance, while the reflecting boundary condition is more appropriate for confined particle systems.

2.3.3. Particle cancelling

During simulations if the z-coordinate of the moving particle is 150 grid points higher than its initial location (i.e., 300 points above the top-surface of the deposit structure), then the particle is cancelled. A new particle is freshly released at the same height of the initial position of the cancelled particle but at a randomly selected horizontal location. This approach involves accelerating the simulation, especially when the diffusion is dominant over other transport mechanisms, where the Peclet number would allow particles to perform unceasing random walks in the 3-D space far away from the deposit surface. Cancelling these particles does not alter any physical properties of the deposit structure but only increases the computational efficiency.

3. Results and discussion

3.1. Trajectory fractal dimension

The dominance of transport mechanisms can be evaluated by the trajectory fractal dimension which is defined as

$$D_{\mathrm{Traj}} = \frac{2}{1+\alpha} \tag{8}$$

for which the following relationship is used:

$$\left\langle (\vec{r} - \vec{r}_0)^2 \right\rangle \propto N_p^{-(1+\alpha)} \tag{9}$$

with

$$\left\langle (\vec{r} - \vec{r}_0)^2 \right\rangle \propto \frac{1}{N_p} \frac{1}{M} \sum_{i=1}^{N_p} \sum_{j=1}^{M} (\vec{r}_{i,j} - \vec{r}_{i,0})^2 \qquad (\vec{r}_{i,j} - \vec{r}_{i,0}) \tag{10}$$

where M is the total number of movement steps, and $\vec{r}_{i,j}$ is the position of the ith particle at time step j, after it was initially released at $\vec{r}_{i,0}$. Theoretically, the averaging over the particle number in Eq. (10) is not necessary, but it significantly accelerates the convergence of the mean variance of particle positions in comparison to a case where a single or a few particles is used for much longer time steps [24].

Fig. 1 shows the variation of the trajectory fractal dimension with respect to the Peclet number, which converges to 2.0 and 1.0 at low ($\leq 10^{-2}$) and high ($\geq 10^{1}$) Peclet number limits, implying diffusion-dominated and convection-dominated transports, respectively. The transition between the two transport mechanisms occurs at a Peclet number on order of O (10^{-1}), below and above which particles move nearly in random and ballistic manners, respectively. This phase transition of mass transport is clarified when the derivative of the trajectory fractal dimension with respect to the Peclet number (in log-scale) is calculated as shown in the bottom graph of Fig. 1. It specifically indicates that the transport transition occurs at $\mathrm{Pe} = 10^{-0.84}$ (=0.146) taken as the peak of the derivative plot, which is fitted using a polynomial expansion.

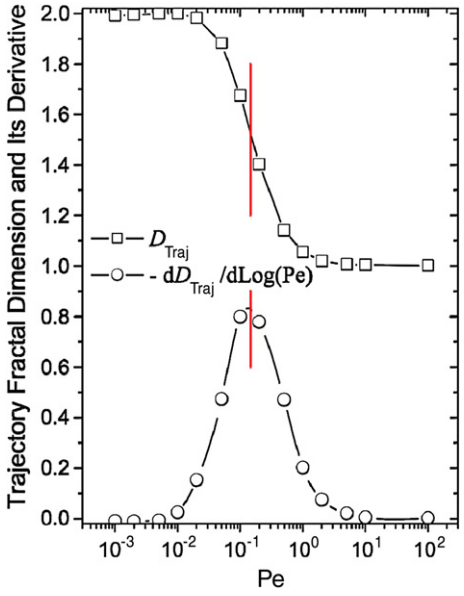

Fig. 1. Trajectory fractal dimension, D_{Traj}, and its negative first order derivative, $-dD_{\mathrm{Traj}}/d\mathrm{Log}(\mathrm{Pe})$. The peak value of the derivative occurs at $\mathrm{Pe} = 10^{-0.84}$ (=0.146) as indicated by the short vertical line and thus divides the diffusion- and convection-limited transports.

3.2. Deposit structures

Final deposit structures are shown in Fig. 2, representing their apparent variations with respect to the Peclet number. Fig. 2(a) shows the deposit structure dominantly grown under diffusion-limited transport with Pe = 0.01, which appears to be very open and sparse. Locally clumped groups are observed, and the top-surface boundary is very rough and hence difficult to delineate. In 2-D simulations of other researchers who used small Peclet numbers [9,13,17,20], deposit structures were observed as tree-like, open, and dendritic with poorly defined top-surfaces. In the 2-D space, diffusing particles have fewer penetration opportunities in to the deposit layer and contribute to more vertically spreading structures (with attenuating density profiles) instead of locally clumped structures in 3-D space. This stems from the fact that movement in 2-D space is geometrically more restricted than that in 3-D space.

Co-existence of the locally clumped and densely packed structures is found in Fig. 2(b) (in comparison to Fig. 2(a)) even though the substrate dimension of Fig. 2(b) is only 50×50 for proper visualization. Later simulations all use the larger dimension of 300×300 for substrate surfaces to provide statistically reliable data.

Densely packed structures, with appearances similar to those of well-packed building blocks, are shown in Fig. 2(c) and (d) for Pe = 1.0 and 10.0, respectively. The structures are formed under convection-limited, ballistic particle transport with high Peclet numbers that cause denser structures than those of Fig. 2(a) and (b). It seems obvious by visually observing Fig. 2(a)–(d) that diffusion and convection/gravitation violently compete with each other to

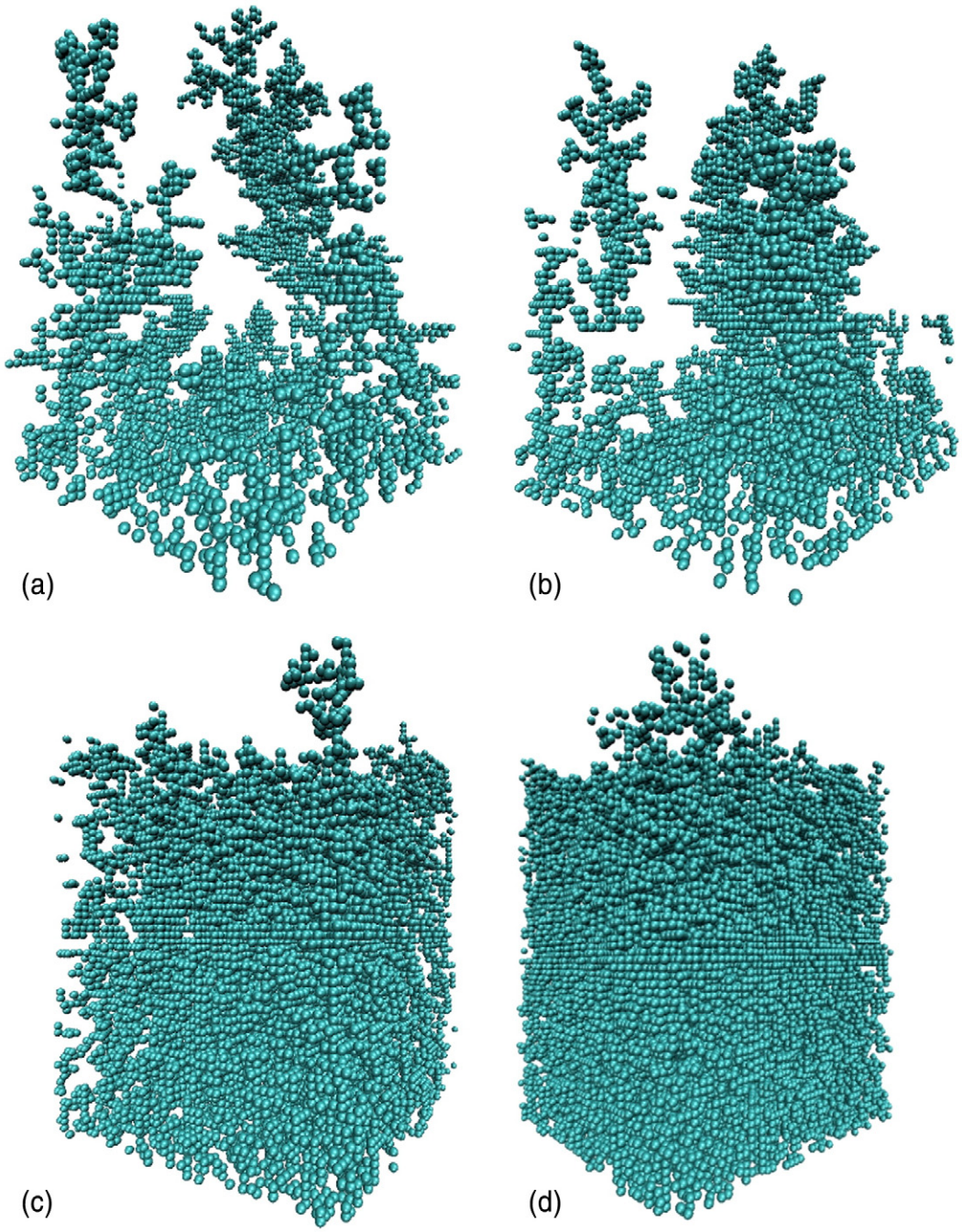

Fig. 2. Sample fractal structures of deposit layers on the substrate for grid dimension 50×50: (a) Pe = 0.01, (b) Pe = 0.1, (c) Pe = 1.0, and (d) Pe = 10.0.

dominate the particle transport near the Peclet number on the order of O (10^{-1}) as supported by the previous analysis of the trajectory fractal dimension in Section 3.1. 2-D projections of these 3-D structures can be well quantified using the lateral density profiles discussed in the next section.

3.3. Lateral density profile

The deposit structure is characterized using lateral density, which represents geometrical variation of the structure along the z-axis, defined as

$$\rho(h) = \frac{\pi d_p^3}{6}\frac{n(h)}{LWd_p} \tag{11}$$

where $n(h)$ is the number of particles deposited at the height, h, with thickness of particle diameter d_p. The height-average of the local number density $\rho(h)$ is equal to the average volume fraction of the entire deposited structure.

The variation of the lateral density along the z-direction is shown in Fig. 3(a) and (b) in terms of the height, h. Three regions are identified for each Peclet number, which are defined in this study as founding, grown, and progressing regions.

- *Founding region*: The local density $\rho(h)$ rapidly decreases after initial deposition of the first group of particles, which form a shallow layer defined as the founding layer. In this region, the declining trend of the local density follows in a power-wise manner as shown in the straight portions in the log–log plots of Fig. 3(a). This power-

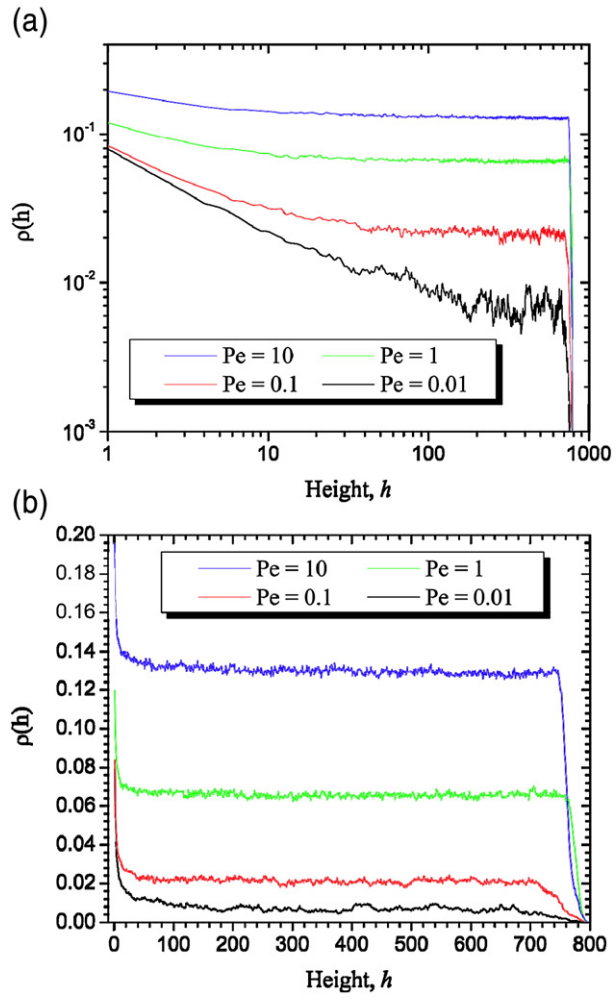

Fig. 3. Variation of lateral density with respect to the structure height based on Peclet number: (a) log–log and (b) linear scale plots.

wise propensity depicted in Fig. 3(b) for short heights (h<100) is more apparent for cases with low Peclet numbers for which the whose founding layers are thicker than those of high Peclet numbers. The early group of particles deposited on the clean permeable surface captures post-depositing particles, prevents particle arrivals at the substrate, and therefore contributes to power-wise decline of the lateral density profile.

- *Grown region*: Once a fractal structure is well formed in the founding region, the plateau stage of the lateral density starts forming. From this time, moving particles can barely reach the permeable substrate since they are captured by and perfectly sunk onto the deposited structure (see Section 2.3). Particles colliding with the top-most particles contribute to the growth of the structure. Due to the presence of the pre-deposited particles, moving particles cannot reach certain locations below a threshold height. The distance between the top-most particle and the threshold height is in this study defined as the penetration depth (see Section 3.5). When the deposit height becomes larger than this penetration depth, the density decline in the z-direction seems to come to a halt and a second region of uniform density starts forming. This phenomenon is here denoted as the structural transition from founding to grown regions.
- *Progressing region*: In addition to the founding region of gradual decline and the grown region of homogeneous density, the progressing region can be identified by the rapid decline of the lateral density toward zero in Fig. 3. The thickness of this progressing region increases with decreasing Peclet number in a similar fashion to that of the founding region. This implies that the random-walk-like particle movement in the diffusion-limited transport generates a thicker founding and progressing region with a sparser structure and lower density.

The three regions discussed here were not distinctly noticed in a previous study [9,13,17,20] probably due to the simulations performed in 2-D space using an insufficient number of particles as a result of computational limitations; and/or the final heights of simulated deposit structures not being tall enough to clearly generate three stratified layers.

3.4. Fractal dimension

A dominant mechanism that governs the particle transport was quantified using the Peclet number, Pe. This mechanism determines the overall shape and average density of the generated structure as shown in Fig. 3. Another fundamental way to investigate the deposit structure is to estimate the structural fractal dimension,[1] defined as

$$D_f = 2 + \frac{1}{\phi} \tag{12}$$

with

$$\overline{h}\left(= \sum_{i=1}^{N_p} z_i \right) \propto N_p^{\phi} \tag{13}$$

where $\overline{h}$ is the mean height of N_p particles, and z_i is the z-coordinate of the ith particle. The length scale for the surface roughness can be quantified using the root-mean-square deviation (RMSD), defined as

$$RMSD = \sqrt{\frac{1}{LW}\sum_{i=1}^{L}\sum_{j=1}^{W}(h_{ij}-\overline{h})^2} \tag{14}$$

where h_{ij} is the position of the top-most particle above the substrate at grid point (i,j). The RMSD varies with the number of deposited particles, N_p, and the mean height, $\overline{h}$, in a power-wise manner, such that

$$RMSD = N_p^{\omega} \tag{15}$$

and

$$RMSD = \overline{h}^{\psi} \tag{16}$$

respectively. Combining Eqs. (13), (15), and (16) for large N_p and tall $\overline{h}$ yields

$$\phi = \frac{\omega}{\psi} \tag{17}$$

and provides an alternative expression of fractal dimension to Eq. (12):

$$D_f = 2 + \frac{\psi}{\omega}. \tag{18}$$

Fig. 4 shows variations of ϕ, ω and ψ versus Peclet number, in which ϕ and ω appear to decrease, and ψ increases with increasing Peclet number. Note that the ϕ values plotted in Fig. 4 are calculated using Eq. (13). It is shown that ψ does not exceed ω, but approaches the lowest value of ω at large Peclet numbers, which confirms that D_f calculated using Eq. (18) is limited to 3.0. (Structural fractal dimensions, independently estimated using Eqs. (12) and (18), are

[1] Distinct from the trajectory fractal dimension of Eq. (8).

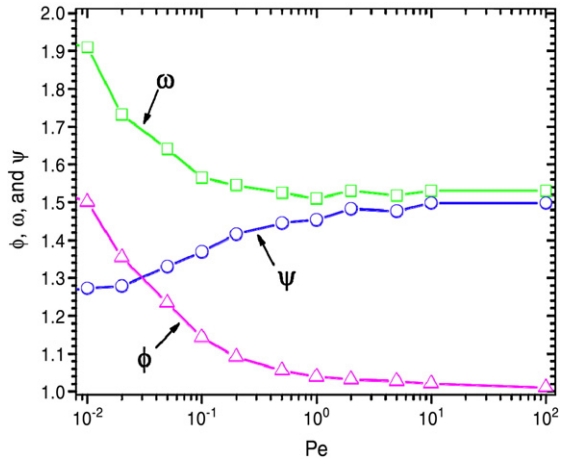

Fig. 4. Variations of ϕ, ω, and ψ (of Eqs. (13), (15), and (16), respectively) versus Peclet number.

almost identical to each other as shown in Fig. 5.) A detailed analysis of Fig. 4 is summarized in Table 1 and explained below.

In the previous discussion, Figs. 2 and 3 prove that the Peclet number controls the physical characteristics of the deposit layer: as the Peclet number increases, it contributes more to ballistic transport and generates denser structures. It can be concluded from Fig. 4 and Eqs. (13) and (15) that $\overline{h}$ and RMSD decrease as the Peclet number increases because ϕ and ω decrease with respect to the Peclet number. This can be physically interpreted as given the number of deposited particles N_p, a higher Peclet number characterizes a deposit structure with a shorter height and smoother (i.e., better-defined) top-surface. On the other hand, Eqs. (13) and (16) indicate that, given the deposit height $\overline{h}$, N_p and RMSD increase with respect to the Peclet number since ψ varies oppositely to the trend of ϕ with increasing Peclet number, as shown in Fig. 4. When two deposit structures have the same average height $\overline{h}'$, one formed with a higher Peclet number has more deposited particles with a rougher top-surface. If the diffusion-limited transport, ascribed to a low Peclet number, generates the forest-like top-surface with a certain mean height, $\overline{h}'$, then there must be summits and valleys, of which the geometrical variation is quantified using the RMSD, denoted here as $\delta_{diffusive}$. When a high Peclet number creates a dense structure with the same mean height of $\overline{h}'$, its RMSD, $\delta_{ballistic}$ is taller

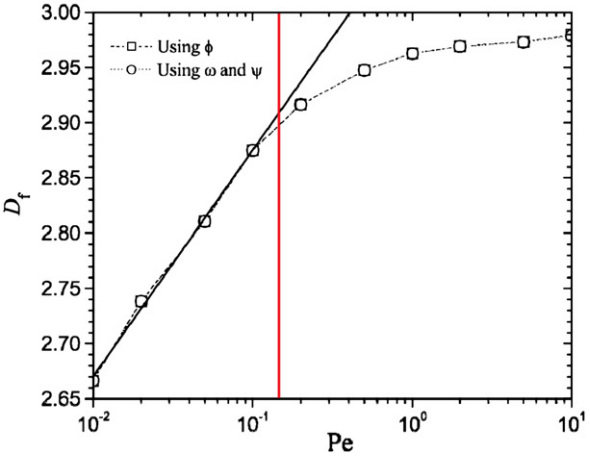

Fig. 5. Structural fractal dimension versus Peclet number. The solid straight line is from the linear regression using the first four points, and the vertical line is the plot of $Pe = 10^{-0.84} = 0.146$ from Fig. 1. Rectangular and circular symbols indicate values of the structural fractal dimension calculated using Eqs. (12) and (18), respectively, for which independent calculations show excellent agreement.

Table 1
Analysis of the effect of the Peclet number on the deposit structure.

	$\overline{h} \propto N_p^{\phi}$ (Eq. (13)) with RMSD $\propto N_p^{\omega}$ (Eq. (15))	$N_p \propto \overline{h}^{1/\phi}$ (Eq. (13)) with RMSD $\propto \overline{h}^{\psi}$ (Eq. (16))
Given	N_p	$\overline{h}$
As Pe (↑),	$\phi(\downarrow)$ and $\omega(\downarrow)$	$\phi(\downarrow)$ and $\psi(\uparrow)$
D_f (↑) and $\langle\rho\rangle$(↑)	$\overline{h}$ (↓) and RMSD(↓)	N_p(↑) and RMSD(↑)

than $\delta_{diffusive}$, confirming the results in Table 1. The ballistic transport produces a structure similar to many long rods vertically aligned and embedded on a soft surface, forming narrow holes between the rods. The structure is characterized as the fractal dimension close to 3.0 as shown in Fig. 5 for large Peclet numbers. Under this circumstance, the x and y coordinates of a particle at the initial position (when released) and final location (after deposition) can be very close to each other.

Fig. 5 shows the range of the structural fractal dimension of objects with finite surface area in 3-D Euclidean space, which is greater than 2 and less than 3. The diffusive and ballistic transports produce fractal deposit layers with $D_f \simeq 2.67$ and 2.98, respectively, confirming the basic idea described above. For low Peclet numbers ($<10^{-1}$), the fractal dimension is logarithmically proportional to the Peclet number as shown by the linear regression in Fig. 5. For high Peclet numbers ($>10^{0}$), the fractal dimension becomes nearly independent of the Peclet number, since the transition probability of Eq. (5) would not substantially change. The deviation point of the fractal dimension from the linear regression starts near $Pe = 10^{-0.84}$, as indicated in Fig. 1. This reconfirms that the particle transport mechanism is the primary influence on the physical characteristics of the deposit structure. A comparison of Figs. 1 and 5 points out that the trajectory fractal dimension can be used as a precursor for estimating the structural fractal dimension as well as the structural phase transition. The offset value of Pe to the horizontal line, $D_f = 3$, can induce the fractal dimension of an extrapolated structural transition from diffusion-limited to ballistic influences. The transition occurs at $Pe = 10^{-0.40}$, which is slightly higher than the transition point of the trajectory fractal dimension, i.e., $Pe = 10^{-0.84}$. The small difference, $10^{-0.40} - 10^{-0.84}$ (=0.25), is attributed to the capturing of particles during drifting movements. An estimation of the trajectory fractal dimension uses numerous particles moving in the 3-D free lattice space in a sufficient number of steps. Before performing enough movements conducive to accurate trajectory fractal dimension, drifting particles are captured within the deposit structure in the intermediate course of their deposition. The stopping of drifting particles is perhaps the main origin of the slight discrepancy between two transitions occurring at $Pe = 10^{-0.84}$ and $10^{-0.40}$, estimated in terms of the trajectory and structural fractal dimensions, respectively.

3.5. Penetration depth

Fig. 6 shows the penetration depth that is calculated as follows. While the deposit layer grows due to continuous particle deposition, the maximum height of the deposit layer, which is equal to the z-coordinate of the top-most particle, is monitored. Whenever the maximum height reaches a multiple of 10, i.e., 10, 20,..., up to 800, 10,000 additional particles are independently released 150 grid points above the maximum height. The difference between the maximum height and the average of the final z-coordinates of the 10,000 particles after deposition is taken as the penetration depth. As expected, an open and sparse structure of lower fractal dimension (stemming from a lower Peclet number) allows a deeper penetration of drifting particles. Revisiting Table 1 for the constant $\overline{h}$ case clarifies the relationship between the RMSD and penetration depth. Although long narrow holes in the vertical direction can significantly contribute to increasing RMSD, the narrowness of holes precludes further particle transport through vertically straight intermediate spaces and therefore diminishes the penetration depth. One can observe from Fig. 6 that the penetration

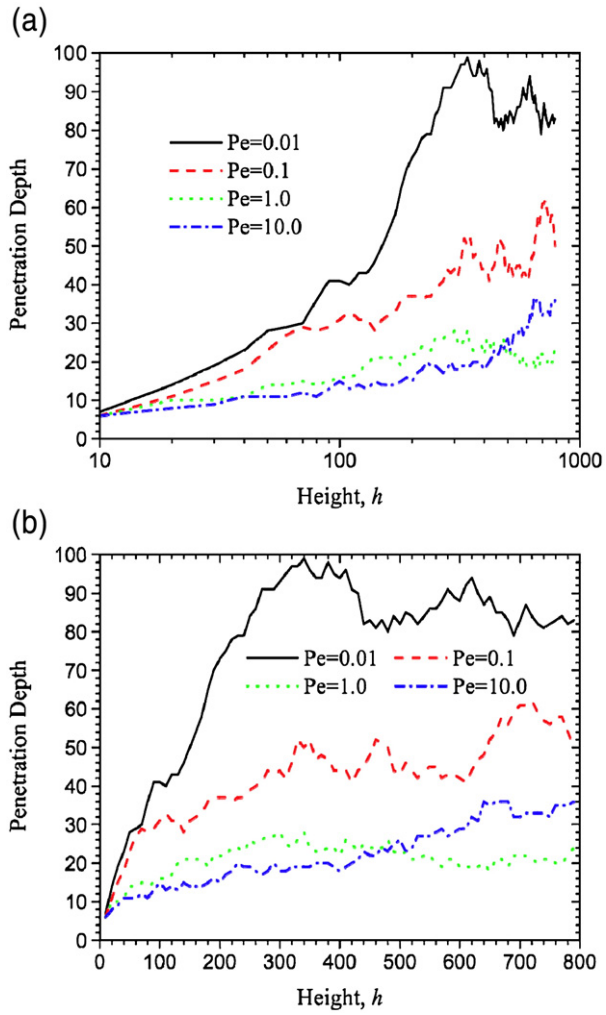

Fig. 6. Penetration depth versus Peclet number with different values of Pe: (a) semi-log and (b) linear scale plots.

depth increases with the structure height in the beginning of the deposition, and later undergoes fluctuation near a certain quasi-constant, especially for low Peclet numbers. A higher penetration depth with lower Peclet numbers is the trade-off with sparser and more open structures that provide larger local spaces for particle drifting; given the structure height, the penetration depth is inversely proportional to the RMSD.

4. Conclusions

The phase transition of the trajectory fractal dimension under the biased influences of convection and gravitation is strongly correlated to the structural phase transition of deposit layers, characterized by the variation of the structural fractal dimension with respect to the Peclet number. Lateral density profiles show three distinct layers of founding, grown, and progressing regions, which have not be observed in previous 2-D simulations. The average density of the deposit layer and its structural fractal dimension are proportional to the Peclet number, which indicates that the ballistic transport generates a denser layer. A lower structural fractal dimension characterizes a sparser structure, of which local open spaces allow drifting particles to penetrate deeper into the structure.

Acknowledgment

This research was supported by a grant from the US National Science Foundation Faculty Early Career (CAREER) Development Program (CBET04-49431).

References

[1] Y. Chen, H. Kim, Monte Carlo simulation of pore blocking and cake formation by interfacial interactions during membrane filtration, Desalination 233 (1–3) (2008) 258–266.
[2] A.S. Kim, Y. Liu, Irreversible chemical potential and shear-induced diffusion in crossflow filtration, Industrial and Engineering Chemistry Research 47 (15) (2008) 5611–5614.
[3] T.D. Waite, A.I. Schafer, A.G. Fane, A. Heuer, Colloidal fouling of ultrafiltration membranes: impact of aggregate structure and size, Journal of Colloid and Interface Science 212 (2) (1999) 264–274.
[4] F.G. Meng, H.M. Zhang, Y.S. Li, X.W. Zhang, F.L. Yang, J.N. Xiao, Cake layer morphology in microfiltration of activated sludge wastewater based on fractal analysis, Separation and Purification Technology 44 (3) (2005) 250–257.
[5] P.K. Park, C.H. Lee, S. Lee, Permeability of collapsed cakes formed by deposition of fractal aggregates upon membrane filtration, Environmental Science & Technology 40 (8) (2006) 2699–2705.
[6] M.M. Sharp, I.C. Escobar, Effects of dynamic or secondary-layer coagulation on ultrafiltration, Desalination 188 (1–3) (2006) 239–249.
[7] A. Bagga, S. Chellam, D.A. Clifford, Evaluation of iron chemical coagulation and electrocoagulation pretreatment for surface water microfiltration, Journal of Membrane Science 309 (1–2) (2008) 82–93.
[8] P. Meakin, Formation of fractal clusters and networks by irreversible diffusion-limited aggregation, Physical Review Letters 51 (13) (1983) 1119–1122.
[9] M. Matsushita, Y. Hayakawa, Y. Sawada, Fractal structure and cluster statistics of zinc-metal trees deposited on a line electrode, Physical Review A 32 (6) (1985) 3814–3816.
[10] T. Vicsek, Fractal Growth Phenomena, World Scientific Pub. Co. Inc, 1992.
[11] F. de los Santos, J.M. Tavares, M. Tasinkevych, M.M.T. da Gama, Diffusion-limited deposition of dipolar particles, Physical Review E 69 (6) (2004) 061406.
[12] A.-L. Barab'asi, H.E. Stanley, Fractal Concepts in Surface Growth, Cambridge University Press, 1995.
[13] S. Veerapaneni, M.R. Wiesner, Particle deposition on an infinitely permeable surface, Journal of Colloid and Interface Science 162 (1) (1994) 110–122.
[14] T.A. Witten, L.M. Sander, Diffusion-limited aggregation, a kinetic critical phenomenon, Physical Review Letters 47 (19) (1981) 1400–1403.
[15] T.A. Witten, L.M. Sander, Diffusion-limited aggregation, Physical Review B 27 (9) (1983) 5686–5697.
[16] L.M. Sander, Z.M. Cheng, R. Richter, Diffusion-limited aggregation in three dimensions, Physical Review B 28 (11) (1983) 6394–6396.
[17] P. Meakin, Diffusion-controlled deposition on surfaces: cluster-size distribution, interface exponents, and other properties, Physical Review B 30 (8) (1984) 4207–4214.
[18] P. Meakin, J.M. Deutch, Monte Carlo simulation of diffusion controlled colloid growth rates in two and three dimensions, The Journal of Chemical Physics 80 (5) (1984) 2115–2122.
[19] P. Bourke, Constrained diffusion-limited aggregation in 3 dimensions, Computers & Graphics 30 (4) (2006) 646–649.
[20] P. Meakin, Diffusion-controlled deposition on fibers and surfaces, Physical Review A 27 (5) (1983) 2616–2623.
[21] G. Redwine, Upgrading to FORTRAN 90, Springer-Verlag, New York, 1995.
[22] V.V. Tarabara, M.R. Wiesner, Effect of collision efficiency on the evolution of the surface of diffusion-limited deposits, Journal of Colloid and Interface Science 237 (1) (2001) 150–151.
[23] V.K. Singh, E.S.G. Shaqfeh, Effect of surface re-emission on the surface roughness of film growth in low pressure chemical vapor deposition, Journal of Vacuum Science & Technology A: Vacuum, Surfaces, and Films 11 (3) (1993) 557–568.
[24] A.S. Kim, H. Chen, Diffusive tortuosity factor of solid and soft cake layers: a random walk simulation approach, Journal of Membrane Science 279 (1–2) (2006) 129–139.